

Imaging the Deep Structures of Los Humeros Geothermal Field, Mexico, Using Three-Component Seismic Noise Beamforming

Katrin Løer^{1,2}, Tania Toledo³, Gianluca Norini⁴, Xin Zhang⁵, Andrew Curtis^{5,6}, and Erik Hans Saenger^{1,7,8}

Abstract

We present a 1D shear-velocity model for Los Humeros geothermal field (Mexico) obtained from three-component beamforming of ambient seismic noise, imaging for the first time the bottom of the sedimentary basement ~ 5 km below the volcanic caldera, as well as the brittle-ductile transition at ~ 10 km depth. Rayleigh-wave dispersion curves are extracted from ambient seismic noise measurements and inverted using a Markov chain Monte Carlo scheme. The resulting probability density function provides the shear-velocity distribution down to 15 km depth, hence, much deeper than other techniques applied in the area. In the upper 4 km, our model conforms to a profile from local seismicity analysis and matches geological structure inferred from well logs, which validates the methodology. Complementing information from well logs and outcrops at the near surface, discontinuities in the seismic profile can be linked to geological transitions allowing us to infer structural information of the deeper subsurface. By constraining the extent of rocks with brittle behavior and permeability conditions at greater depths, our results are of paramount importance for the future exploitation of the reservoir and provide a basis for the geological and thermodynamic modeling of active superhot geothermal systems, in general.

Cite this article as Løer, K., T. Toledo, G. Norini, X. Zhang, A. Curtis, and E. H. Saenger (2020). Imaging the Deep Structures of Los Humeros Geothermal Field, Mexico, Using Three-Component Seismic Noise Beamforming, *Seismol. Res. Lett.* **91**, 3269–3277, doi: [10.1785/SR202000022](https://doi.org/10.1785/SR202000022).

[Supplemental Material](#)

Introduction

Los Humeros volcanic complex (LHVC; Fig. 1), located in the eastern part of the Trans-Mexican volcanic belt (TMVB), hosts a conventional geothermal field (Ferrari *et al.*, 2012; Gutiérrez-Negrín, 2019). On-going hydrothermal activity makes the LHVC a favorable area for geothermal exploitation, and a geothermal power plant has been operating since the 1990s. The LHVC has been identified as an important natural laboratory for the development of general models of superhot geothermal systems (SHGSs) in volcanic calderas (e.g., Jolie *et al.*, 2018).

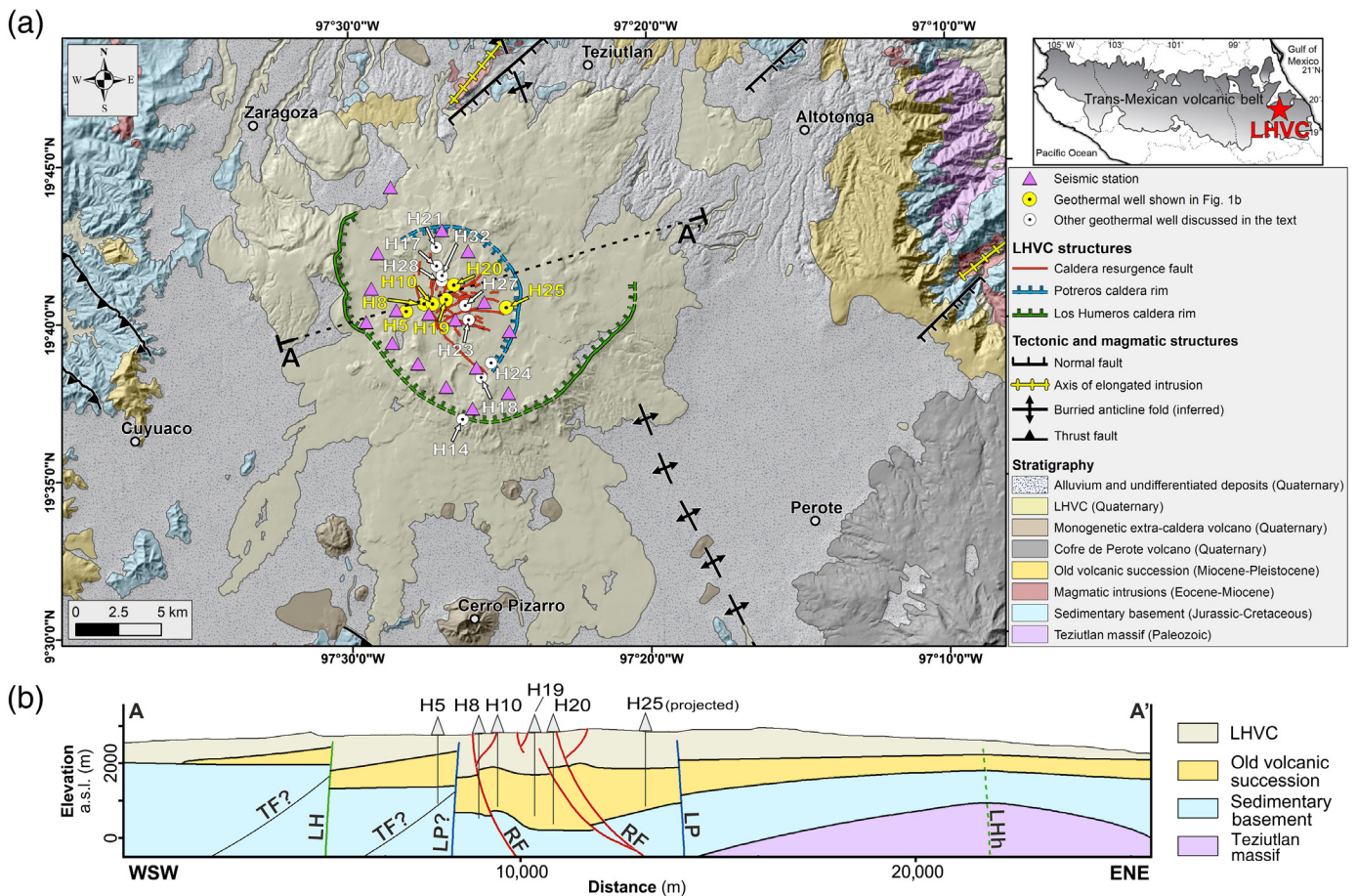
Although extensive geological field studies and well log analyses have provided many constraints on the near-surface geology of the caldera complex and conventional geothermal reservoir, conditions at depths greater than 2–3 km are largely unknown and currently being studied intensively (Jolie *et al.*, 2018). It is assumed that superhot fluids could exist in the carbonate rock basement underlying the caldera (Jolie *et al.*, 2018). These rocks might exhibit secondary permeability related to the damage zone of active resurgence faults and inherited pervasive basement structures (Lorenzo-Pulido, 2008; Rocha-López *et al.*, 2010; Norini *et al.*, 2015, 2019;

Jolie *et al.*, 2018). The maximum depth of these brittle structures is defined by the brittle-ductile (BD) transition zone, which thus plays an important role in geothermal exploration because upper crustal faults and fractures behave as hydraulic channels for the circulation of geothermal fluids (e.g., Ranalli and Rybach, 2005). In SHGSs that exhibit a positive thermal anomaly, the depth of the BD transition may differ from areas with a normal thermal gradient, as rocks become progressively more ductile with increasing temperature. Thus, a positive

1. Department of Civil and Environmental Engineering, Bochum University of Applied Sciences, Bochum, Germany; 2. Now at Department of Geology and Geophysics, University of Aberdeen, Aberdeen, United Kingdom; 3. German Research Centre for Geosciences GFZ, Section 4.8 Geoenergy, Section 2.2 Geophysical Deep Sounding, Potsdam, Germany; 4. Istituto di Geologia Ambientale e Geoingegneria, Consiglio Nazionale delle Ricerche, Area della Ricerca CNR—ARM3, Milan, Italy; 5. School of Geosciences, Grant Institute, University of Edinburgh, Edinburgh, United Kingdom; 6. Institut für Geophysik, ETH Zürich, Zürich, Switzerland; 7. Institut für Geologie, Mineralogie und Geophysik, Ruhr-Universität Bochum, Bochum, Germany; 8. Fraunhofer-Einrichtung für Energieinfrastruktur und Geothermie IEG, Bochum, Germany

*Corresponding author: katrin.loer@hs-bochum.de; katrin.loer@abdn.ac.uk

© Seismological Society of America



thermal anomaly could potentially limit the volume of rocks in which secondary permeability may exist.

We use three-component (3C) beamforming to extract structural information from ambient seismic noise. 3C beamforming is an array technique, which, like standard beamforming, not only estimates the dominant propagation direction and wavenumber of a recorded wavefield, but in addition determines the polarization of the wavefield by comparing phase shifts across different components (Riahi *et al.*, 2013). As a result, different wave types can be distinguished and their propagation parameters analyzed separately. This allows us, for example, to estimate wavefield composition and surface-wave anisotropy, which is, however, beyond the scope of this study. Here, we consider fundamental mode Rayleigh waves only and extract dispersion curves from frequency–wavenumber (f - k) histograms; these are inverted for a shear-velocity depth profile using a reversible-jump Markov chain Monte Carlo (rj-McMC) algorithm. Although this algorithm is computationally expensive, it has the advantage of providing uncertainties for the velocity profile by finding the distribution of models that are consistent with data.

3C beamforming does not require impulsive (man-made or natural) seismic sources and is thus cheap, flexible, and applicable also in aseismic areas. Whereas cross-correlation-based ambient noise methods typically rely on month-long

Figure 1. (a) Simplified geological map of the Los Humeros volcanic complex (LHVC) and surrounding basement, on a shaded relief. The trace of the A–A' geological cross section of panel (b) is shown. Triangles denote seismic station locations of the dense broadband (DB) network, circles denote geothermal wells. In the upper-right inset, the location of the LHVC within the Trans-Mexican volcanic belt (TMVB) is indicated. (b) A–A' schematic geological cross section showing the subsurface geometry of the main structures and stratigraphic units. Trace of the geological cross section is shown in panel (a). Modified from Norini *et al.* (2019). ENE, east-northeast; LH, Los Humeros caldera ring fault; LHh, inferred flexure plane of the Los Humeros trap-door caldera; LP, Los Potreros caldera ring fault; TF: thrust fault; RF, resurgence fault (red lines); WSW, west-southwest. The color version of this figure is available only in the electronic edition.

recordings, from beamforming, we extract stable dispersion curves from only 1 day of seismic noise data. Depending on the array geometry and seismic noise spectrum, the depth sensitivity of 3C beamforming can exceed that of other seismic methods by several kilometers, as we will show in this study. The analysis of four reflection seismic lines recorded across the LHVC, for example, provided 2D velocity maps and seismic sections down to 6 km at the most (Jousset, Ágústsson, *et al.*, 2019). Ambient noise cross-correlation methods applied in the same area, but using a larger array, produce 3D tomographic

images down to a maximum of 10 km depth (Granados Chavarria *et al.*, 2020; Martins *et al.*, 2020). In a similar manner, a recent local earthquake tomography study provides information only of the upper 3–4 km (Toledo *et al.*, 2020). We show that 3C beamforming provides information to greater than 10 km depth.

In the following, we describe geology and available datasets, introduce both 3C beamforming and the *rj*-MCMC inversion algorithm, and summarize our findings in Los Humeros and their implications for SHGSs, in general.

Geology of LHVC

The LHVC basement is composed of Mesozoic sedimentary rocks involved in the Late Cretaceous–Eocene compressive orogenic phase that generated the Mexican fold and thrust belt (sedimentary basement unit in Fig. 1) (Fitz-Díaz *et al.*, 2017; references therein). The sedimentary basement rests above the Precambrian–Paleozoic crystalline basement of the Teziutlan Massif unit, made of greenschists, granodiorites, and granites (e.g., Suter, 1987; Suter *et al.*, 1997; Ortuño-Arzate *et al.*, 2003; Ángeles-Moreno, 2012; Fitz-Díaz *et al.*, 2017) (Fig. 1a,b). Since the Eocene, the area underwent a limited extensional tectonic phase, associated with northeast-striking normal faults and the emplacement of Eocene–Miocene granite and granodiorite magmatic intrusions (Fig. 1a). The TMVB volcanic activity occurred from 10.5 to 1.55 Ma with the emplacement of fractured andesites, basaltic lava flows, and few volcanoclastic levels (old volcanic succession unit in Fig. 1) (e.g., Yanez and Garcia, 1982; Ferriz and Mahood, 1984; López-Hernández, 1995; Cedillo-Rodríguez, 1997; Carrasco-Núñez, Hernandez, *et al.*, 2017; Carrasco-Núñez *et al.*, 2018). Volcanic activity resumed ~700 ka ago with the emplacement of the Pleistocene–Holocene LHVC (LHVC unit in Fig. 1) (e.g., Carrasco-Núñez, Hernandez, *et al.*, 2017; Carrasco-Núñez *et al.*, 2018). This volcanic complex represents a basaltic andesite–rhyolite system of two nested calderas, namely the outer Los Humeros caldera and the inner Los Potreros caldera (Carrasco-Núñez, Hernandez, *et al.*, 2017; Calcagno *et al.*, 2018) (Fig. 1a). The LHVC caldera stage occurred between ~165 and ~69 ka and consisted of two major caldera-forming events that emplaced more than 100 km³ of ignimbrite deposits (Yanez and Garcia, 1982; Ferriz and Mahood, 1984; Carrasco-Núñez, Hernandez, *et al.*, 2017; Carrasco-Núñez *et al.*, 2018). Widespread postcaldera monogenetic volcanic activity and resurgence of Los Potreros caldera floor occurred since 50 ka (Norini *et al.*, 2015, 2019) (Fig. 1a).

The conventional geothermal field under exploitation is located in Los Potreros caldera, in the area deformed by resurgence faults (Fig. 1a), and is hosted by the Miocene–Pleistocene andesites, sealed by the LHVC ignimbrite deposits and/or the upper part of the pre-LHVC volcanic units (e.g., Cedillo-Rodríguez, 1997; Arellano *et al.*, 2003; Norini *et al.*, 2015, 2019; Carrasco-Núñez, Lopez-Martinez, *et al.*, 2017). The permeability in the conventional reservoir is mainly secondary,

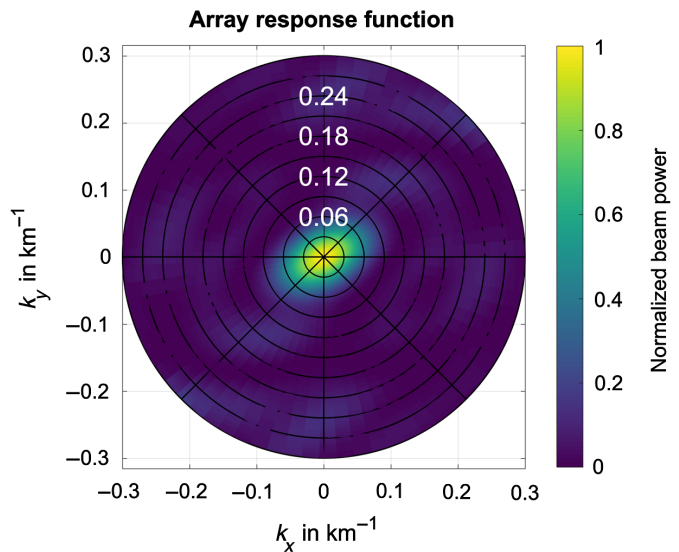


Figure 2. Array response function of the DB seismic array shown in Figure 1a in the wavenumber domain. The color version of this figure is available only in the electronic edition.

generated by volcanotectonic faults and inherited tectonic structures (e.g., Cedillo-Rodríguez, 1997; Arellano *et al.*, 2003; Norini *et al.*, 2015, 2019) (Fig. 1). At the surface, hydrothermal alteration of recent volcanic rocks is exposed along most of the volcanotectonic fault scarps, in which sharp thermal anomalies have been identified by remote sensing (Norini *et al.*, 2015, 2019). The maximum temperature of the hydrothermal fluids is around 400°C, measured at approximately 2.5 km depth (Arellano *et al.*, 2003; Lorenzo-Pulido, 2008; Rocha-López *et al.*, 2010).

Data and Methods

Seismic array and data processing

A multipurpose, temporary seismic array was installed across the LHVC, which recorded continuously from September 2017 to 2018 (see Data and Resources; Toledo *et al.*, 2019). It consisted of 45 3C stations, 25 broadband and 20 short period stations, centered around previously located microseismic events within the inner caldera. For ambient noise beamforming, we use up to 17 stations of the dense broadband (DB) array (triangles in Fig. 1a) with a frequency sensitivity down to below 0.01 Hz and a sampling rate of 200 Hz. The analysis was restricted to 10 days in October and November 2017, when at least 14 stations were operating and dispersion curves had good quality. The corresponding array response function gives the beam response for a wave coming from directly below the array (with wavenumber $k = 0$) and is shown in Figure 2.

Data processing is carried out following Riahi *et al.* (2013) and Löer *et al.* (2018). Data are downsampled to 10 Hz, band-pass filtered between 0.01 and 1 Hz, and cleared from linear trends. We apply spectral whitening and one-bit normalization in the time domain to suppress large amplitude signals from

earthquakes and to equalize amplitudes across different stations. Although time-domain normalization removes absolute amplitude information, we found that it significantly improved the extraction of Rayleigh-wave dispersion curves compared to other methods tested. Time series are divided into short windows, which are then beamformed separately. The length of a single time window corresponds to four times the minimum period, rounded up to the next power of two to speed up Fourier transformation. To this end, data are processed in three frequency bins, 0.08–0.155, 0.160–0.310, and 0.315–0.430 Hz, with corresponding time-window lengths of 51.2, 25.6, and 12.8 s, respectively. This way, the relative time-window length with respect to frequency is kept constant and, compared to a constant absolute time-window length, the number of superimposed waves, especially for larger frequencies, is reduced. Afterward, an average beam response of 10 consecutive time windows is computed.

3C beamforming

In standard, vertical-component beamforming, the horizontal wavenumber k , and the azimuth θ of a wavefield recorded at an array are estimated by analyzing phase shifts of the signal recorded at different stations within a small time and frequency window (Rost and Thomas, 2002). When 3C data are available, one can also analyze the phase shift between different components of each station and thereby estimate the orientation of particle motion of the dominant wave, hence its polarization (e.g., Riahi et al., 2013; L er et al., 2018). In this case, the beam response is computed as a function of three parameters, namely the horizontal wavenumber k and the azimuth θ , combined in the horizontal wavenumber vector

$$\mathbf{k} = k \begin{pmatrix} \cos \theta \\ \sin \theta \end{pmatrix}, \quad (1)$$

and the so-called polarization state ξ , according to

$$R^{3C}(\mathbf{k}, \xi) = \mathbf{w}(\mathbf{k}, \xi) \times \mathbf{S}^{3C} \times \mathbf{w}(\mathbf{k}, \xi)^\dagger. \quad (2)$$

All operations are performed in the frequency domain for a single frequency ω ; the frequency dependence is dropped in all equations for brevity. In equation (2), \mathbf{S}^{3C} represents the cross-spectral density matrix of 3C array data in the frequency domain, and

$$\mathbf{w}(\mathbf{k}, \xi) = \mathbf{c}(\xi) \otimes \mathbf{a}, \quad (3)$$

is the Kronecker product of phase shifts $\mathbf{c}(\xi)$ and $\mathbf{a}(\mathbf{k})$, caused by polarization and wavenumber vector, respectively. Quantity

$$\mathbf{a}(\mathbf{k}) = \frac{1}{\sqrt{M}} \begin{bmatrix} \exp(i\mathbf{k} \times \mathbf{r}_1) \\ \vdots \\ \exp(i\mathbf{k} \times \mathbf{r}_M) \end{bmatrix}, \quad (4)$$

is an M -dimensional vector (Riahi et al., 2013), in which $[\mathbf{r}_1, \mathbf{r}_2, \dots, \mathbf{r}_M]$ denote the M different station locations of the array. It is related to the array response vector

$$A(\mathbf{k}) = \frac{1}{M} \sum_{m=1}^M \exp(i\mathbf{k} \times \mathbf{r}_m), \quad (5)$$

known from standard beamforming. $\mathbf{c}(\xi)$ is a complex 3×1 vector representing the polarization ellipse parameterized by $\xi = \xi(\theta, \phi, \epsilon, \gamma)$. The four polarization parameters denote azimuth (θ), dip (ϕ), ellipticity (ϵ), and tilt (γ) of a wave's particle motion. For more details, see Riahi et al. (2013) and L er et al. (2018). The maximum of the beam response $R^{3C}(\mathbf{k}, \xi)$ gives the parameter combination (k , θ , and ξ) that matches the parameters of the actual wavefield best.

The resolvable wavenumber range is restricted by the geometry of the array (the minimum and maximum interstation distances d_{Min} and d_{Max} , and the location of stations with respect to one another). A first estimate is obtained using an approximation for the resolvable wavelength λ ,

$$2d_{\text{Min}} < \lambda < 3d_{\text{Max}}, \quad (6)$$

(Tokimatsu, 1997), and transferring it to wavenumber:

$$\frac{1}{3d_{\text{Max}}} < k < \frac{1}{2d_{\text{Min}}}. \quad (7)$$

For Los Humeros DB array with $d_{\text{Min}} = 1.6$ km and $d_{\text{Max}} = 13.9$ km, this results in $0.02 \text{ km}^{-1} < k < 0.31 \text{ km}^{-1}$. We note, however, that the wavenumber sensitivity is slightly azimuthally dependent due to the irregular aperture of the array, as can be seen in the array response function (Fig. 2). Ambient noise tomography (ANT) based on cross correlations requires interstation distances larger than one typical wavelength, that is, $\lambda < d$ (e.g., Luo et al., 2015). That means, using the same seismic array, larger wavelengths and hence deeper structures can be investigated using ambient noise beamforming compared to ANT.

From horizontal wavenumber k surface-wave phase velocity c can be computed from $c = f/k$. Otherwise, by estimating minimum and maximum local phase velocities c_{Min} and c_{Max} , wavenumber limits can be transferred to frequency limits, according to

$$c_{\text{Max}} \cdot k_{\text{Min}} < f < c_{\text{Min}} \cdot k_{\text{Max}}. \quad (8)$$

Taking $c_{\text{Min}} = 1.5 \text{ km s}^{-1}$ and $c_{\text{Max}} = 4.5 \text{ km s}^{-1}$ and using the wavenumber limits from equation (7), we obtain a resolvable frequency range of $0.11 \text{ Hz} < f < 0.47 \text{ Hz}$ for surface waves.

In our analysis, we use discrete frequency steps of $\Delta f = 0.005$ Hz. The wavenumber is limited to $k_{\text{Max}} = 0.3 \text{ km}^{-1}$ and sampled at discrete intervals of $\Delta k = 0.0015 \text{ km}^{-1}$ in agreement with the resolution constraints of the array. The azimuth is sampled counterclockwise from east in 5° steps. The incidence angle varies between 0° (vertical) and 90° (horizontal) in 10° steps for body waves and is constant (90°) for surface waves.

Dispersion curve retrieval and inversion

In a medium in which velocities change with depth, surface waves are dispersive, that is, different frequencies propagate at different velocities, since they oscillate at different depths. Using ambient noise beamforming, we measure frequency-dependent Rayleigh-wave phase velocities, which are displayed as dispersion curves representing velocity as a function of frequency. Dispersion curves are extracted from 2D f - k histograms, showing how often a specific wavenumber was measured at a specific frequency for a given time window and polarization. Histograms of consecutive time windows are stacked up to 1 day. Figure 3a shows one such histogram for Rayleigh-wave polarization on day 300 in 2017. From the daily wavenumber histograms, we extract the maximum of the distribution at each frequency, which yields a curve $k(f)$. Using $c = f/k$, we then transfer it from the wavenumber to the phase velocity domain. Taking the average of multiple daily curves, we compute a mean curve and its standard deviation (Fig. 3b), downsampled to $\Delta f = 0.2$ Hz for a faster application of the inversion scheme.

The average dispersion curve is inverted using a Bayesian inversion scheme. Bayesian inversions are performed using the method of rj-McMC (Green, 1995; Bodin *et al.*, 2012). These methods update a prior probability distribution that describes information about model parameters that is independent of the current data, with the new information added by that data. This process is known as Bayesian inference, and the result is a posterior distribution over parameters. The rj-McMC algorithm performs the update while allowing the number and depth extent of seismic velocity parameters of horizontally layered media (and hence the dimensionality of parameter space) to vary in the inversion. The parameterization is adapted to only the complexity required by the combination of prior information and data, which improves results on otherwise high-dimensional nonlinear inverse problems. The resulting probability density function (PDF) provides the distribution of models that are consistent with the data.

Prior information about seismic shear velocities is assigned to be a uniform distribution between $500 \text{ m s}^{-1} < v_s < 7500 \text{ m s}^{-1}$, and the number of layers in depth is allowed to vary between 5 and 25, with the maximum depth constrained to 30 km. Each run of rj-McMC then generates a chain of two million samples (example velocity models), which are distributed according to the posterior distribution as the

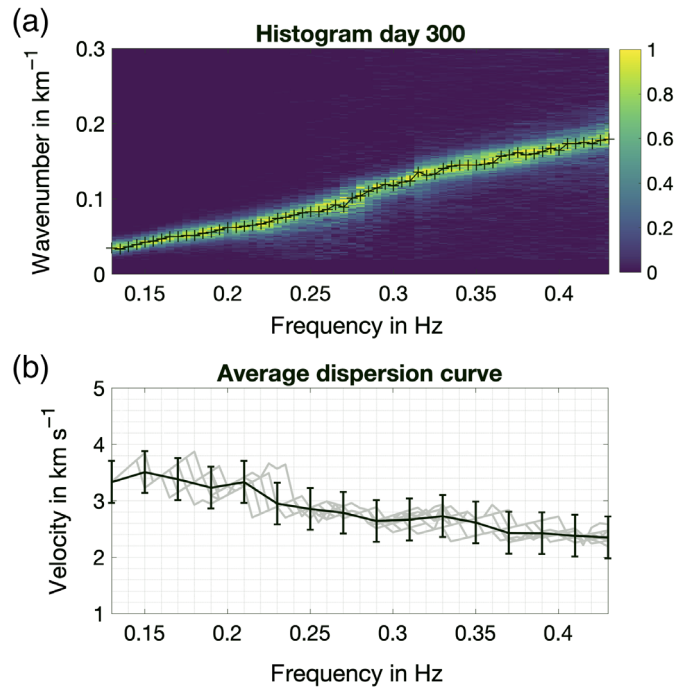


Figure 3. (a) 2D histogram showing wavenumber versus frequency of retrograde Rayleigh-wave detections on day 300 (2017), normalized per frequency. Black crosses mark wavenumber bins with maximum number of detections per frequency, $k(f)$. (b) Average dispersion curve (black) providing phase velocity as a function of frequency, $c(f)$, computed from 10 daily dispersion curves (gray), and downsampled to $\Delta f = 0.2$ Hz. Black error bars indicate twice the average standard deviation. The color version of this figure is available only in the electronic edition.

number tends to infinity. The rj-McMC inversion scheme is run multiple times (here, 12 chains in total), each starting from a different random model. To obtain approximately independent samples, we retain only every 250th sample after the first 0.5 million samples (the “burn-in” phase) in each chain for analysis. The density of the final set of retained samples represents the PDF of shear velocity with depth.

Results

Figure 4a shows the PDF of shear velocity as a function of depth, in which the zero level equals 2.9 km above sea level, that is, the average topographic height of the seismic stations considered. Dimensions are 500×100 grid points, with a grid spacing of $\Delta z = 62 \text{ m}$ in z direction and about $\Delta v_s = 71 \frac{\text{m}}{\text{s}}$ in x direction. For each grid point, the number of samples indicates the number of models that assign a certain shear velocity to the respective depth. The color scale has been normalized with respect to the maximum number of samples at each depth level. Light colors indicate velocities of higher probability compared to dark colors. The solid white curve denotes the maximum likelihood of the PDF, the dashed curve is the mean of

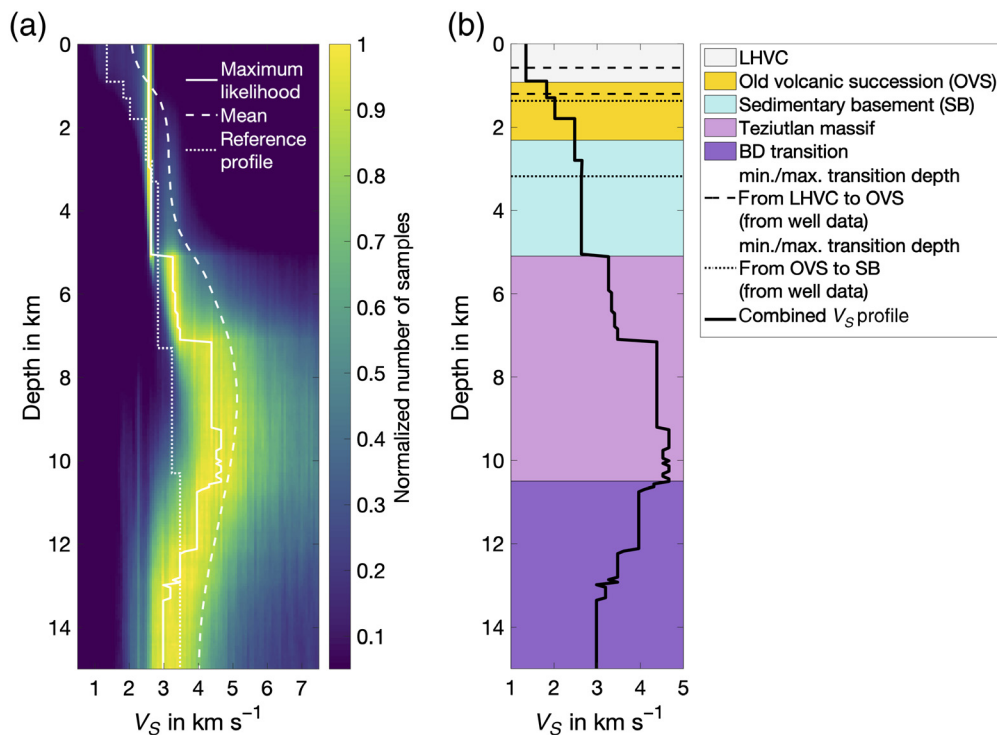


Figure 4. (a) Probability density function (PDF) of shear-velocity distribution, as retrieved from reversible-jump Markov chain Monte Carlo (rj-MCMC) inversion, normalized per depth level. The solid curve indicates maximum likelihood of the PDF, the dashed line is the mean and the dotted curve represents the profile retrieved from the analysis of earthquake data. (b) Combined shear-velocity profile (black) from the analysis of earthquake data (dotted curve in panel (a), down to 3.2 km depth) and ambient noise beamforming (solid curve in panel (a), below 3.2 km); background colors indicate geological structure (see legend) as in Figure 1b. Transition depths are derived from well data for the two upper sections (see Table S1) and from the shear-velocity PDF for the deeper structures. Dashed and dotted horizontal lines indicate the range of transition depths found in well data. BD, brittle-ductile. The color version of this figure is available only in the electronic edition.

the PDF, and the dotted white curve shows the shear-velocity profile obtained from earthquake analysis for comparison (T. Toledo, personal comm., 1 June 2020). The latter was estimated using the code Velest (Kissling *et al.*, 1994) for joint inversion for *P*- and *S*-wave models using travel-time data from 333 local seismic events.

In Figure 4b, we display a shear-velocity profile that combines the results from both methods: down to 3.2 km, it is based on earthquake data (dotted curve in Fig. 4a); below 3.2 km, it follows ambient noise beamforming results (solid curve in Fig. 4a). The earthquake-based profile is reliable mostly in the upper few kilometers, because seismicity was restricted down to a maximum of 6 km below the surface with over 80% of all events occurring above 3.2 km (see Fig. S1 in supplemental material available to this article for depth distribution). Below this depth, it reflects the initial input model. For the noise-based profile, given the frequency limits discussed in the *Seismic Array and Data Processing* section, surface waves are expected to be the most sensitive to depths between 2

and 12 km (see Fig. S1 for sensitivity kernels). For depths between 2 and 4 km, both profiles are in good agreement. Laterally, they provide average velocities for the area covered by the DB array.

Background colors in Figure 4b indicate different geological sections. For the LHVC and the old volcanic succession, section transitions correspond to average transition depths observed in well logs at 0.9 and 2.2 km, respectively (see Table S1 and Norini *et al.*, 2019). Deeper section transitions could not be observed in well logs and are thus derived from discontinuities in the shear-velocity profile.

At 5.1 km depth, shear velocities increase abruptly from around 2.6 to 3.3 km s⁻¹, implying the transition from the sedimentary to the crystalline basement (the Teziutlan massif), which so far has only been mapped at the surface west-northwest of the central caldera (Fig. 1a). Laboratory values for *S*-wave velocities at respective pressure conditions confirm a range between 2.5

and 3.1 km s⁻¹ for limestones and between 3.2 and 3.6 km s⁻¹ for granites and granodiorites (Gebrande, 1982). Bär and Weydt (2019) performed ultrasonic pulse velocity measurements at rock samples from Los Humeros geothermal wells, reporting *S*-wave velocities between 2.2 and 3.6 km s⁻¹ at an average of 3.4 km s⁻¹ for limestones at surface temperature. With increasing temperature, they show that *S*-wave velocities decrease to about 1.5 km s⁻¹ at 400°C.

At about 7 km depth, the velocity profile shows another sudden increase of shear velocity, which could indicate a geological boundary within the generally heterogeneous Teziutlan massive (Yanez and Garcia, 1982; Ángeles-Moreno, 2012) or an intrusive body never identified before. We note, however, that the PDF exhibits a relatively broad velocity distribution (Fig. 4a) at and below that depth and that also the mean curve implies a considerable uncertainty with respect to depth and magnitude of the discontinuity. Thus, a more gradual velocity change related to increasing pressure conditions seems equally likely.

The decline in shear velocity observed at about 10.5 km depth is interpreted as the onset of the BD transition, which correlates with a decrease in shear strength (e.g., Imber *et al.*, 2008). This transition marks the maximum depth for the occurrence of brittle structures that could facilitate secondary permeability.

Discussion and Conclusions

Analyzing ambient seismic noise data, we have imaged for the first time the bottom depth of the sedimentary basement and the BD transition zone in the area of Los Humeros geothermal field. We used 3C beamforming to retrieve Rayleigh-wave dispersion curves from noise data, which were then inverted to give a shear-velocity profile using an rj-McMC algorithm. The profile complements results from earthquake-based methods, which are in good agreement with geological data obtained from well logs; however, these methods provide information only down to a maximum of ~4 km. The depth sensitivity of our method extends down to 15 km, covering the transition from the sedimentary to the crystalline basement in 5 km depth and the BD transition zone around 10 km depth.

Generally, rocks become progressively more ductile with depth because of the increasing temperature, until the BD transition is reached (Ranalli and Rybach, 2005). Our results demonstrate for the first time in the LHVC area that even if the geothermal gradient is higher than for normal crust (e.g., Arellano *et al.*, 2003; Lorenzo-Pulido, 2008; Rocha-López *et al.*, 2010), and if alteration of the rocks hosting the hydrothermal fluids occurs with an expected reduction of the total rock strength (e.g., Arzate *et al.*, 2018; Norini *et al.*, 2019), both sedimentary succession (sedimentary basement unit in Figs. 1 and 4) and upper part of the underlying crystalline basement (Teziutlan Massif unit in Figs. 1 and 4) exhibit a brittle rheology down to 10 km below the topographic surface. The 10 km deep BD transition acts as the root zone of brittle structures responsible for secondary permeability in the geothermal reservoir and potentially hosting superhot fluids. The rheological zonation identified at 10 km below surface should thus be included in any geological model of the caldera complex and hydrothermal system, as well as in heat flow and heat transfer modeling (e.g., Calcagno *et al.*, 2019).

One way to verify our results would be to test them against receiver functions, which are generally used to investigate the near-surface structure using body-wave energy from distant sources that have been refracted and converted at layers beneath a seismometer (Phinney, 1964; Vinnik, 1977). Galetti and Curtis (2012) showed that the theories of receiver functions and seismic interferometry are closely connected, and that the former could also be computed from ambient noise sources and across different stations. To show this, however, is beyond the scope of this work and will be subject to future research.

We provide an estimate of the BD transition depth at 10 km that is independent from local seismicity, since our shear-

velocity profile has been estimated from ambient noise. Our results confirm that declining seismicity below 3.2 km depth is not caused by the transition from brittle to ductile rheology; instead, it is related to the maximum exploitation depth of the geothermal field. Seismicity studies at LHVC prior to exploitation activities have been minimum (Ponce and Rodríguez, 1977), with most studies being accomplished during the exploitation phase (e.g., Lermo *et al.*, 2008). These studies along with a more recent survey (Gaucher *et al.*, 2019; Jousset, Toledo, *et al.*, 2019; Toledo *et al.*, 2020) show minimum local seismicity mostly related to the geothermal field activities. In fact, earthquakes at LHVC occur mostly in clusters located close to injection wells. Some of these events have depths larger than the injection wells (~2.5 km depth) and are located in the limestones belonging to the sedimentary basement unit, suggesting possible local fracturing of this layer due to pressure changes caused by injection and production activities. The heterogeneous focal mechanisms (mostly strike slip with left- and right-lateral motion) (Lermo *et al.*, 2008) and the temporal relation of the seismicity rate with injection rates (Lermo *et al.*, 2008; Jousset, Toledo, *et al.*, 2019) seem to confirm that parts of the local seismicity is induced by local stresses due to injection. Another part of the seismicity is of tectonic origin.

The presented shear-velocity model may also help to constrain boundary conditions for other methods. For example, it can be used as a starting model for 3D seismic tomography (Gaucher *et al.*, 2019; Toledo *et al.*, 2020), in earthquake localization with time-reverse imaging (Werner and Saenger, 2018) or for assessing the correlation between rock moduli and temperature (Mendrinós *et al.*, 2019).

Overall, we demonstrate that 3C beamforming of ambient noise combined with dispersion curve inversion using the rj-McMC algorithm provides information on deeper structures of SHGSs that is typically not found by standard methods such as well log or seismicity analysis. Based on ambient seismic noise, the method is also applicable in aseismic regions where other methods are altogether infeasible. It complements ambient noise cross-correlation-based techniques, which, while providing 3D tomographic images, require a significantly larger array aperture to reach the same depth sensitivity and are computationally much more expensive. 3C beamforming provides a quick first estimate of deep geological structures from a 1D seismic profile, which can also serve as initial model for other methods. Our findings in the LHVC suggest that SHGSs can exhibit brittle rheology at large depths, despite positive thermal anomalies, increasing the rock volume available for geothermal exploitation.

Data and Resources

Waveform data and associated metadata are available from the GEOFON data center under network code 6G (<https://geofon.gfz-potsdam.de/doi/network/6G/2017>, last accessed March 2019) and

are embargoed until January 2023. The Comisión Federal de Electricidad (CFE) of Mexico kindly provided logs of geothermal wells and access to the geothermal concession area. Cartographic data are stored in a personal geodatabase, and the final map of Figure 1 was produced in ESRI ArcMap 10.3. The supplemental material for this article includes a figure showing the depth sensitivity kernels of Rayleigh waves compared to the depth distribution of local seismicity (Fig. S1) and a table listing geothermal wells and transition depths of geological units identified in the corresponding well logs (Table S1).

Acknowledgments

The research leading to these results has received funding from the GEMex Project, funded by the European Union's Horizon 2020 research and innovation program under Grant Agreement Number 727550, and by the Mexican Energy Sustainability Fund CONACYT-SENER, WP 4.5 of the Project 2015-04-268074. Katrin Løer has received funding from the German Research Foundation (DFG) under Project Number 298820846. The authors acknowledge Gerardo Carrasco-Núñez for useful discussions on the geology of Los Humeros volcanic complex (LHVC) and the Comisión Federal de Electricidad (CFE) personnel for their support during the study of the geothermal field. The authors also thank Benedikt Ahrens for valuable contributions to the interpretation of the velocity profile.

References

Ángeles-Moreno, E. (2012). *Geological Map of the Western Border of the Cuicateco Terrane, Southern Mexico*, Geological Society of America, Boulder, Colorado, MCH102 (1 sheet).

Arellano, V. M., A. Garcia, R. M. Barragan, G. Izquierdo, A. Aragon, and D. Nieva (2003). An updated conceptual model of the Los Humeros geothermal reservoir (Mexico), *J. Volcanol. Geother. Res.* **124**, 67–88.

Arzate, J., F. Corbo, G. Carrasco-Núñez, J. Hernández, and V. Yutsis (2018). The Los Humeros (Mexico) geothermal field model deduced from new geophysical and geological data, *Geothermics* **71**, 200–211.

Bär, K., and L. Weydt (2019). Comprehensive report on the rock and fluid samples and their physical properties in the Acoculco and Los Humeros regions, Deliverable D6.1, WP6, GEMex H2020 project, European Commission, available at <http://www.gemex-h2020.eu> (last accessed June 2020).

Bodin, T., M. Sambridge, H. Tkalcic, P. Arroucau, K. Gallagher, and N. Rawlinson (2012). Transdimensional inversion of receiver functions and surface wave dispersion, *J. Geophys. Res.* **117**, no. B2, doi: [10.1029/2011JB008560](https://doi.org/10.1029/2011JB008560).

Calcagno, P., G. Evanno, E. Trumpy, L. C. Gutiérrez-Negrín, J. L. Macías, G. Carrasco-Núñez, and D. Liotta (2018). Preliminary 3-D geological models of Los Humeros and Acoculco geothermal fields (Mexico)—H2020 GEMex Project, *Adv. Geosci.* **45**, 321–333.

Calcagno, P., E. Trumpy, L. C. Gutiérrez-Negrín, G. Norini, J. L. Macías, G. Carrasco-Núñez, D. Liotta, V. Garduño-Monroy, G. P. Hersir, L. Vaessen, *et al.* (2019). Updating the 3D Geomodels of Los Humeros and Acoculco Geothermal Systems (Mexico)—H2020 GEMex Project, *World Geothermal Congress 2020*, Reykjavik, Iceland, 21–26 May 2021, available at <https://hal-brgm.archives-ouvertes.fr/hal-02268392/document> (last accessed July 2020).

Carrasco-Núñez, G., J. P. Bernal, P. Davila, B. Jicha, G. Giordano, and J. Hernandez (2018). Reappraisal of Los Humeros volcanic complex by new U/Th zircon and ⁴⁰Ar/³⁹Ar dating: Implications for greater geothermal potential, *Geochem. Geophys. Geosyst.* **19**, 132–149.

Carrasco-Núñez, G., J. Hernandez, L. De Leon, P. Davila, G. Norini, J. P. Bernal, and P. Lopez (2017). Geologic map of Los Humeros volcanic complex and geothermal field, eastern Trans-Mexican volcanic belt, *Terra Digitalis* **1**, no. 2, 1–11.

Carrasco-Núñez, G., M. Lopez-Martinez, J. Hernandez, and V. Vargas (2017). Subsurface stratigraphy and its correlation with the surficial geology at Los Humeros geothermal field, eastern Trans-Mexican volcanic belt, *Geothermics* **67**, 1–17.

Cedillo-Rodríguez, F. (1997). *Geología del subsuelo del campo geotermico de Los Humeros, Puebla, Internal Rept. HU/RE/03/97*, Comisión Federal de Electricidad, Gerencia de Proyectos Geotermoelectricos, Residencia Los Humeros, Puebla, Mexico.

Ferrari, L., T. Orozco-Esquivel, V. Manea, and M. Manea (2012). The dynamic history of the Trans-Mexican volcanic belt and the Mexico subduction zone, *Tectonophysics* **522**, 122–149.

Ferriz, H., and G. Mahood (1984). Eruptive rates and compositional trends at Los Humeros volcanic center, Puebla, Mexico, *J. Geophys. Res.* **89**, 8511–8524.

Fitz-Díaz, E., T. F. Lawton, E. Juárez-Arriaga, and G. Chávez-Cabello (2017). The Cretaceous–Paleogene Mexican orogen: Structure, basin development, magmatism and tectonics, *Earth Sci. Rev.* **183**, 56–84.

Galetti, E., and A. Curtis (2012). Generalised receiver functions and seismic interferometry, *Tectonophysics* **532**, 1–26.

Gaucher, E., T. Toledo, M. Metz, A. G. Figueroa-Soto, and M. Calò (2019). One year of passive seismic monitoring of the Los Humeros (Mexico) geothermal field, *European Geothermal Congress 2019*, Den Haag, The Netherlands, 11–14 June 2019, available at <http://www.gemex-h2020.eu> (last accessed July 2020).

Gebrande, H. (1982). *Elastic Wave Velocities and Constants of Elasticity of Rocks and Rock-forming Minerals (Subvolume B: Landolt-Börnstein—Group V Geophysics)*, Springer, Berlin/Heidelberg.

Granados Chavarria, I., M. Calò, Á. Figueroa Soto, and P. Jousset (2020). 3D Anisotropic velocity model of the Los Humeros geothermal field, Mexico, using seismic ambient noise tomography, *EGU General Assembly 2020*, Online, 4–8 May, doi: [10.5194/egusphere-egu2020-12544](https://doi.org/10.5194/egusphere-egu2020-12544).

Green, P. J. (1995). Reversible jump Markov chain Monte Carlo computation and Bayesian model determination, *Biometrika* **82**, no. 4, 711–732.

Gutiérrez-Negrín, L. C. A. (2019). Current status of geothermal-electric production in Mexico, *IOP Conf. Ser. Earth Environ. Sci.* **249**, no. 1, 012017.

Imber, J., R. E. Holdsworth, S. A. F. Smith, S. P. Jefferies, and C. Collettini (2008). Frictional-viscous flow, seismicity and the geology of weak faults: A review and future directions, *Geol. Soc. Lond. Spec. Publ.* **299**, no. 1, 151–173.

Jolie, E., D. Bruhn, A. L. Hernández, D. Liotta, V. H. Garduño-Monroy, M. Lelli, G. P. Hersir, C. Arango-Galván, D. Bonté, P. Calcagno, and P. Deb (2018). GEMex—A Mexican–European Research Cooperation on Development of Superhot and Engineered Geothermal Systems, *43rd Workshop on Geothermal Reservoir Engineering Stanford University*, Stanford, California, 12–14 February 2018, available at <https://pangea.stanford.edu/>

<ERE/pdf/IGAstandard/SGW/2018/Jolie2.pdf> (last accessed July 2020).

- Jousset, P., K. Ágústsson, E. Barison, G. Böhm, M. Caló, I. G. Chavarría, B. Farina, E. Gaucher, K. Loer, J. Martín, *et al.* (2019). Seismic structures of the Acochulco and Los Humeros geothermal fields, Deliverable D5.3, WP5, GEMex H2020 project, European Commission, available at <http://www.gemex-h2020.eu> (last accessed July 2020).
- Jousset, P., T. Toledo, C. Finger, K. Löer, and E. H. Saenger (2019). Time dependent processes within the Mexican fields, Deliverable D5.4, WP5, GEMex H2020 project, European Commission, available at <http://www.gemex-h2020.eu> (last accessed June 2020).
- Kissling, E., W. L. Ellsworth, D. Eberhart-Phillips, and U. Kradolfer (1994). Initial reference models in local earthquake tomography, *J. Geophys. Res.* **99**, no. B10, 19,635–19,646.
- Lermo, J., Y. Antayhua, L. Quintanar, and C. Lorenzo (2008). Estudio sísmológico del campo geotérmico de Los Humeros, Puebla, México. Parte I: Sismicidad, mecanismos de fuente y distribución de esfuerzos, *Geotermia, Rev. Mex. Geoenerg.* **21**, no. 1, 25–41 (in Spanish).
- Löer, K., N. Riahi, and E. H. Saenger (2018). Three-component ambient noise beamforming in the Parkfield area, *Geophys. J. Int.* **213**, no. 3, 1478–1491.
- López-Hernández, A. (1995). Estudio Regional Volcánico y Estructural del Campo Geotérmico de Los Humeros, Pue., Mexico, *Geotermia, Rev. Mex. Geoenerg.* **11**, no. 1, 17–36 (in Spanish).
- Lorenzo-Pulido, C. D. (2008). *Borehole geophysics and geology of well H-43, Los Humeros geothermal field, Puebla, México, Geothermal Training Program Rept. 23*, Orkustofnun, Reykjavík, Iceland.
- Luo, Y., Y. Yang, Y. Xu, H. Xu, K. Zhao, and K. Wang (2015). On the limitations of interstation distances in ambient noise tomography, *Geophys. J. Int.* **201**, no. 2, 652–661.
- Martins, J., A. Obermann, A. Verdel, and P. Jousset (2020). 3D-S wave velocity model of the Los Humeros geothermal field, Mexico, by ambient-noise tomography, *EGU General Assembly 2020*, 4–8 May, doi: [10.5194/egusphere-egu2020-21956](https://doi.org/10.5194/egusphere-egu2020-21956).
- Mendrinós, D., S. Karytsas, C. Karytsas, F. Poletto, and B. Farina (2019). Report on distribution of rock modulus and correlation with temperature, Deliverable D5.11, WP5, GEMex H2020 project, European Commission, available at <http://www.gemex-h2020.eu> (last accessed June 2020).
- Norini, G., G. Carrasco-Núñez, F. Corbo-Camargo, J. Lermo, J. Hernández Rojas, C. Castro, M. Bonini, D. Montanari, G. Corti, G. Moratti, *et al.* (2019). The structural architecture of the Los Humeros volcanic complex and geothermal field, *J. Volcanol. Geoth. Res.* **381**, 312–329.
- Norini, G., G. Gropelli, R. Sulpizio, G. Carrasco-Núñez, P. Dávila-Harris, C. Pelliccioli, F. Zucca, and R. De Franco (2015). Structural analysis and thermal remote sensing of the Los Humeros volcanic complex: Implications for volcano structure and geothermal exploration, *J. Volcanol. Geoth. Res.* **301**, 221–237.
- Ortuño-Arzate, S., H. Ferket, M. C. Cacas, R. Swennen, and F. Roure (2003). Late cretaceous carbonate reservoirs in the Cordoba platform and Veracruz Basin, eastern Mexico, in *The Circum-Gulf of Mexico and the Caribbean: Hydrocarbon Habitats, Basin Formation, and Plate Tectonics*, C. Bartolini, R. T. Buffler, and J. F. Blickwede (Editors), Vol. 79, Chapter 22, American Association of Petroleum Geologists Memoir, Tulsa, Oklahoma, 476–514.
- Phinney, R. A. (1964). Structure of the Earth's crust from spectral behavior of long-period body waves, *J. Geophys. Res.* **69**, no. 4, 2997–3017.
- Ponce, L., and Y. C. Rodríguez (1977). Microearthquake activity associated to Los Humeros caldera, Mexico: Preliminary survey, *Geof. Int.* **17**, no. 4, 461–478.
- Ranalli, G., and L. Rybach (2005). Heat flow, heat transfer and lithosphere rheology in geothermal areas: Features and examples, *J. Volcanol. Geoth. Res.* **148**, 3–19.
- Riahi, N., G. Bokelmann, P. Sala, and E. H. Saenger (2013). Time-lapse analysis of ambient surface wave anisotropy: A three-component array study above an underground gas storage, *J. Geophys. Res.* **118**, no. 10, 5339–5351.
- Rocha-López, S., G. Ramírez-Silva, E. Jiménez-Salgado, and C. Lorenzo-Pulido (2010). Results of geological-geophysics drilling of the well H-43 the geothermal field in Humeros, Puebla, Mexico, *World Geothermal Congress 2010*, Bali, Indonesia, 25–29 April 2010, available at <https://www.geothermal-energy.org/pdf/IGAstandard/WGC/2010/1210.pdf> (last accessed July 2020).
- Rost, S., and C. Thomas (2002). Array seismology: Methods and applications, *Rev. Geophys.* **40**, no. 3, 2-1–2-27.
- Suter, M. (1987). Structural traverse across the Sierra Madre oriental fold-thrust belt in east-central Mexico, *Bull. Geol. Soc. Am.* **98**, 249–264.
- Suter, M., J. Contreras-Pérez, and H. Ochoa Camarillo (1997). Structure of the Sierra Madre oriental fold-thrust belt in east-central-Mexico, in *II Convención Sobre la Evolución Geológica de México, Libro-guía de Las Excursiones Geológicas, Excursión 2*, Universidad Autónoma del Estado de Hidalgo; Instituto de Geología, Universidad Nacional Autónoma de México, Pachuca, México, 45–63.
- Tokimatsu, K. (1997). Geotechnical site characterization using surface waves, *1st International Conf. on Earthquake Geotechnical Engineering*, Vol. 3, Balkema, Rotterdam, 1333–1368.
- Toledo, T., E. Gaucher, M. Metz, M. Caló, A. Figueroa, J. Angulo, P. Jousset, K. Kieling, and E. H. Saenger (2019). Dataset of the 6G seismic network at Los Humeros, 2017–2018, GFZ Data Services, Other/Seismic Network, Potsdam, Germany, doi: [10.14470/1T7562235078](https://doi.org/10.14470/1T7562235078).
- Toledo, T., P. Jousset, E. Gaucher, H. Maurer, C. Krawczyk, M. Caló, and A. Figueroa (2020). Local earthquake tomography at the Los Humeros geothermal field, Mexico, EGU General Assembly 2020, Online, 4–8 May 2020, EGU2020-9865, doi: [10.5194/egusphere-egu2020-9865](https://doi.org/10.5194/egusphere-egu2020-9865).
- Vinnik, L. P. (1977). Detection of waves converted from P to SV in the mantle, *Phys. Earth Planet. In.* **15**, no. 1, 39–45.
- Werner, C., and E. H. Saenger (2018). Obtaining reliable source locations with time reverse imaging: limits to array design, velocity models and signal-to-noise ratios, *Solid Earth* **9**, no. 6, 1487–1505.
- Yanez, C., and S. García (1982). *Exploración de la región geotérmica Los Humeros-Las Derrumbadas, Internal Rept. 29/82*, Estados de Puebla y Veracruz, Comisión Federal de Electricidad, Mexico City, Mexico, 98 pp.

Manuscript received 17 January 2020
Published online 5 August 2020